

N 7 1 - 2 8 9 4 6

NASA TM X-67870

**NASA TECHNICAL
MEMORANDUM**

NASA TM X-67870

**INLET-ENGINE-NOZZLE WIND
TUNNEL TEST TECHNIQUES**

by D. N. Bowditch
Lewis Research Center
Cleveland, Ohio

**CASE FILE
COPY**

TECHNICAL PAPER proposed for presentation at
Thirty-eighth Meeting of the Propulsion and Energetics
Panel of the Advisory Group for Aerospace
Research and Development
Sandeford, Norway, September 13-17, 1971

INLET-ENGINE-NOZZLE WIND TUNNEL TEST TECHNIQUES

by

D. N. Bowditch

Lewis Research Center

National Aeronautics and Space Administration

Cleveland, Ohio

SUMMARY

Experimental investigations of the inlet, engine and exhaust nozzle of a supersonic propulsion system have been underway at the Lewis Research Center. Exhaust nozzle results are presented which compare wind tunnel and flight results and assess the accuracy of flight measurements. Comparisons are also presented for nozzle performance obtained with a cold jet, a powered turbojet simulator, and a solid jet boundary simulator. The effect of the local boundary layer on nozzle performance is also discussed. The need for good dynamic measurements during inlet-engine testing is illustrated for transients such as inlet unstart and engine stall. Also, the transient nature of inlet distortion and its effect on the engine is presented for two different operating conditions.

SYMBOLS

A_n	nacelle cross sectional area
C_g	gross thrust coefficient, $T-D/T_{ip}$
$C_{D\beta}$	boattail drag coefficient, D_β/qA_n
D	drag
D_β	boattail drag
d_n	nacelle diameter
d_c	cowl lip diameter
M_0	free stream Mach number
M_2	compressor face Mach number
$N/N_D \sqrt{\theta}$	corrected portion of design engine speed
P_0	free stream total pressure
P_2	compressor face total pressure
\bar{P}_2	average compressor face total pressure
P_3	compressor exit total pressure
ΔP_{2rms}	root mean square value of dynamic component of compressor face pressure
$\overline{\Delta P_{2rms}}$	average value of ΔP_{2rms}
p_2	compressor face static pressure
p_{2max}	maximum compressor face static pressure during hammershock after surge
q	dynamic pressure
r	rounded boattail radius
T	thrust
T_{ip}	ideal primary thrust
α	angle of attack
σ	standard deviation

INTRODUCTION

Within existing ground test facilities experimental investigation of the aircraft propulsion system can rarely be done under the exact conditions that will exist in flight. Facilities are normally too small or models become too complex to simulate the actual flight conditions. Therefore, compromises are necessary and these must be made in such a way that their effect is negligible, or understood well enough so that the results can be corrected properly. Several experimental programs in this area of supersonic propulsion systems are currently underway at the Lewis Research Center, references 1-3.

Much testing of supersonic exhaust nozzles is required at off design speeds corresponding to high subsonic and transonic flight conditions. The geometry of a large area ratio nozzle that is efficient at supersonic pressure ratios of 20 and 30 must be changed at subsonic conditions in order to operate efficiently at much lower pressure ratios of 2 to 4. Collapsing the nozzle normally exposes a boattail or opens inlets on the nozzle which makes it a potential source of drag and the resulting performance is very sensitive to external flow conditions. These problems are investigated in the 8- by 6-foot wind tunnel using isolated nacelle models and subscale aircraft models. In addition, to overcome the size limitations of transonic wind tunnel testing, a flight test program utilizing underwing nacelles on an F-106 aircraft was initiated as illustrated in figure 1. This permits tests of a wide variety of complex nozzles on a complete aircraft configuration that is similar to that required for a supersonic cruise aircraft. The aircraft testing technique and its accuracy will be reviewed as well as several comparisons with wind tunnel data on similar configurations. Several other wind tunnel test techniques will also be described.

In the 10×10 supersonic propulsion wind tunnel, recent inlet-engine test programs have investigated the propulsion system stability and its integration with the airframe. Dynamic considerations are of primary importance in understanding the system operation under conditions such as inlet unstart, engine stall and high distortion. If the significance of the dynamic response of the propulsion system is not recognized, system instabilities may be encountered which could have been avoided by proper measurement and interpretation of dynamic conditions. To study the inlet-engine compatibility problem, several supersonic mixed-compression inlets have been tested with J-85 turbojet engines at Mach 2.5 cruise conditions. Highlights from these tests are used to demonstrate the test techniques used and the considerations necessary to properly evaluate the large-scale dynamic interactions of the propulsion system and airframe.

EXHAUST NOZZLE TESTING

Typical models used for exhaust nozzle testing in the 8×6 foot wind tunnel are shown in figure 2. The isolated nacelle model is used to investigate external flow effects on nozzles. Separate primary and secondary flows are provided through the strut from an external source. The model is of sufficient length that the nozzle performance is not influenced by the disturbances caused by the closed nose of the nacelle and by the support strut at high subsonic speeds. Unfortunately it also provides an undesirably thick boundary layer. The two aircraft models are 5% and, 22% scale models of the F-106 aircraft. The smaller model has been used to investigate the effect of various nacelle shapes and results from those tests indicated the engine accessory bump had negligible effect on boattail drag. Because of transonic tunnel blockage limitations, the flow through nacelles were about 3 centimeters in diameter, and only capable of investigating simple boattails which simulated a variable flap ejector nozzle. The larger 22% scale model had a powered turbojet simulator in the underwing nacelle allowing both inlet and exhaust nozzle flows to be simulated. The model was also large enough to permit investigation of more complex exhaust nozzles. This model is large enough to cause concern about transonic wind tunnel wall interference, and comparison with F-106 flight data is being used to verify the interference-free speed range.

The smaller model utilized a cylindrical tube as a jet boundary simulator since a realistic jet was not practical for such small scale. This concept has been investigated on the isolated jet exit model where the boattail drag was measured with a fully expanded cold air jet and a cylindrical jet boundary simulator, reference 4. Results from that test are compared on figure 3. The drag coefficient of a sharp-edged 15° boattail is presented as a function of free-stream Mach number. The dashed and solid lines represent the drag for a fully expanded jet and jet-off respectively. The data symbols are

for the drag with a jet boundary simulator and it is obvious that the simulator is a good representation of a flowing jet for this case where the flow over the boattail was attached and well behaved.

Since model testing is obviously limited by transonic wind tunnel interference considerations, the F-106 flight test program was initiated at Lewis to permit investigation of propulsion systems at transonic speeds, references 5-8. The research nacelles are illustrated in figure 4. Two J85-13 afterburning turbojet engines are housed in nacelles under the aircraft wings. The nacelle location is typical of supersonic cruise aircraft, with the exhaust nozzle extended just beyond the trailing edge of the wing. The installation permits study of complex installed exhaust nozzles at relatively large size and at transonic speeds. The installation is also being used to make flyby noise measurements to determine flight velocity effects on the effectiveness of jet noise suppressors. This aircraft is particularly useful for this type of work because it is easy to make major changes in nozzle geometry and because a complete data system is available onboard the aircraft to monitor engine and aircraft operating conditions.

The method of nozzle evaluation is illustrated in figure 4. The nacelle is supported by a parallelogram linkage with a load cell restraining the nacelle along its axis to measure the net thrust minus drag. An accelerometer is used to determine any components of nacelle weight or inertia forces aligned with the thrust axis. The drag of the nacelle forward of the nozzle attachment station was evaluated throughout the aircraft operating envelope using a reference nozzle. The internal performance of this nozzle was calibrated and the drag of the well-defined base region was easily obtained with a few pressure measurements. The calibrated nacelle drag is added to the load cell reading of net thrust minus drag to determine research nozzle thrust minus drag. In order to evaluate nozzle performance, the primary conditions must be accurately determined. This was done by calibration of the J-85 engines in an altitude test facility prior to flight testing. Primary flow is obtained in flight testing by combining the airflow from the compressor calibration with the measured fuel flows. The nozzle total pressure and temperature were obtained from measurements at the turbine exit and an afterburner calibration of temperature rise and pressure drop. The ideal thrust of this primary flow is then compared with the measured thrust minus drag of the nozzle. Reference nozzle flights were performed at several times during the program to initially evaluate nacelle drag and later to evaluate system repeatability. The measurement accuracy of nozzle performance on the F-106 was determined from these flights, reference 9, and is presented in figure 5. The table contains the influence coefficient for each parameter on the nozzle gross thrust, C_g , the standard deviation for each parameter and the resulting standard deviation for the gross thrust coefficient. The standard deviation for each of the parameters was estimated by combining standard deviations of calibrations and required instrument accuracies. The resulting standard deviation of nozzle gross thrust coefficient of about one and one-half percent is consistent with observed data scatter.

In order to develop a testing technique that uses a model large enough to accommodate a powered turbojet simulator, the 22% scale F-106 model was tested. The model is shown installed in the 8x6 supersonic wind tunnel in figure 6. The total frontal area of the half-plane model was 1.8 percent of the wind tunnel cross sectional area and the splitter plate and supports added another percent blockage to that. The wing of the model is mounted on a multi-component balance and the nacelle is mounted to the wing on a thrust balance. A powered turbojet simulator is mounted in the nacelle where it provided simulation of both the J-85 inlet and exhaust nozzle flows.

A cutaway drawing of the turbojet simulator is shown in figure 7. It is designed to simulate a modern supersonic turbojet engine. The six-stage axial flow compressor provides a peak pressure ratio of 3.5. The compressor and turbine flows, which are matched in pressure and temperature, join just downstream of the turbine. Makeup air can be added to the resulting primary stream to provide the higher weight flows required to simulate afterburner operation. Secondary air is furnished by a third pipe for testing ejector nozzles. These pipes are mounted rigidly to the simulator, and are housed in the wing. They are connected to fixed mounts outside the wind tunnel by flexible connectors to permit thrust measurement.

A comparison of data from the three sources - flight, 5% scale, and 22% scale - is shown in figures 8 and 9. Sharp edged 15° boattail drag coefficients for the 5% scale model and flight data are compared with isolated values in figure 8. The installation effect of delaying the drag rise for the sharp edged boattail is obvious. Also the agreement of the model and flight data is very good except in the

region of Mach 1.0. The 5% scale data utilized cylindrical jet boundary simulators representing a fully expanded jet. The aircraft nozzle did not become fully expanded until slightly above Mach 1.0 which explains some of the difference between the two sets of data.

The nozzle gross thrust coefficient for a variable flap ejector nozzle is compared for the 22% scale model and flight, figure 9. This performance was derived from nacelle force measurements in both cases. Agreement is very good at subsonic Mach numbers less than 0.9. However, at higher speeds the flight thrust coefficient initially increases and then drops quickly at Mach 0.95 as the nacelle terminal shock passes over the nozzle. On the wind tunnel model, this shock movement was apparently delayed until a Mach number greater than 1.0. Above Mach 1.1 the agreement is only fair.

To illustrate the problems encountered in testing a complex nozzle, consider the auxiliary inlet ejector nozzle shown in figure 10. For this nozzle, part of the exit area variation required for efficient operation at all speeds is obtained by collapsing the trailing overlapping flaps and seals. The remaining area is too large for low pressure ratio operation, and doors are opened to provide air to fill the annulus between the primary jet and the leaves. To save actuator weight, these flaps and doors are positioned by the aerodynamic forces on the nozzle. Because the nozzle contains many complex moving parts, the tendency is to test with the boattail or doors fixed. This can lead to optimistic results are shown on figure 11, where the nozzle gross thrust coefficient is presented over a range of pressure ratios for several combinations of fixed and floating hardware. The best performance is obtained if the inlet doors and trailing flaps are fixed in the desired positions. If only the doors are allowed to float, they partially close, which reduces the thrust about 4 percent. Floating both the doors and flaps, reduces the performance an additional one to 3 percent depending on pressure ratio. Exact duplication of the floating linkage must be made to properly evaluate off-design performance. Another aspect of floating nozzles requiring similar investigation is the stability of the floating system. There are so many possible oscillation modes that testing the floating hardware is the only positive way to evaluate stability.

Another aspect of the nozzle flow field that is difficult to evaluate is the boundary layer. On many exit models used in tunnel testing the boundary layer is too thick due to excessive length or too low Reynolds number. In addition, the boundary layer is not uniformly thick at the nozzle when it is installed at the rear of an aircraft. It is nearly impossible to duplicate the actual installed condition. The effect of boundary layer thickness on boattail drag is presented in figure 12 and is discussed further in reference 10. In the case of both a sharp-edged boattail and a more rounded boattail, increasing boundary-layer thickness reduced drag. In this case, the thicker boundary layer appeared to effectively round the boattail corner thus reducing the drag.

A different problem is presented by the boattails in figure 13. These were designed with final angles of 24° and were to operate near to but without separation. They were investigated inflight on the F-106 aircraft at different altitudes to obtain Reynolds number effects. Case I and II were the same boattail with Case I extended farther beyond the wing trailing edge. Case III is a completely rounded boattail. Figure 14 shows that for all three boattails, the drag decreased as Reynolds number increased. Since boundary-layer thickness should be smaller relative to the body at higher Reynolds number, this is just the opposite of the previous case. By studying tuft pictures and boattail pressure distributions, it was possible to determine that separation regions on the boattails were decreasing with increasing Reynolds number. Therefore, the drag decrease was due to less separation in this case, causing drag to decrease with decreasing boundary-layer thickness. It is therefore necessary to determine the detailed flowfield causing drag before deciding how Reynolds number for boundary-layer thickness) will affect the drag.

DYNAMIC INLET-ENGINE TESTING

The Mach 2.5 mixed-compression inlet and J-85 engine installation used for propulsion system investigations is shown in figure 15. The inlet centerbody translates for inlet starting and for off-design Mach number operation. Bypass doors just ahead of the engine face provide control of the terminal shock position. Bleed is provided on the cowl and also on the centerbody where it is exhausted through support struts. Dynamic pressure measurements have been made at the compressor face with six 5-tube rakes, at the compressor exit, and throughout the inlet and compressor.

To investigate large transients for an axisymmetric nacelle located under a wing, the inlet-engine system was mounted just below a wing simulator (ref. 11) as shown in figure 16. Because of test section size limitations on the length of the simulator, it is difficult to obtain a thick enough boundary layer to simulate some engine installations, so the protuberances at the leading edge of the plate were used to artificially thicken the boundary layer. As described in more detail in reference 12, the desired momentum decrement was obtained with the leading-edge protuberances. The resulting boundary-layer profile near the leading edge was near separation, but was predicted to be well developed when it reached the area of interest ahead of the inlet. Separation tests with a forward-facing step showed it to be separated by a pressure rise almost exactly equal to that required for separation of a natural plate boundary layer. The location of the inlet relative to the plate is shown in more detail in figure 17. The cowl lip was tested at several heights equal to and larger than the boundary-layer height.

When the inlet unstarts, the shock system travels farthest forward during the initial transient. Several pictures from a movie of such a transient are presented in figure 18. These pictures show only the upper cowl lip and top half of the spike cone and the plate and boundary layer above the inlet. From these figures, it can be seen that the inlet shock system progresses clear to the spike tip during the transient, and also separates the plate boundary layer which transmits the disturbance even farther forward. The maximum extent of such a disturbance will determine how widely an adjacent nacelle must be separated in order to avoid one inlet unstart from disturbing an adjacent inlet. Either nacelle separation or some containment of the disturbance by fences must be used to prevent communication of disturbance between nacelles.

The extent of the unstart disturbance on the wing was measured by transient pressure instrumentation, and is presented in figure 19. Inlet unstart from different operating conditions cause variations in the extent of the disturbance. Without an engine installed, the inlet was unstarted by closing the bypass doors and forcing the terminal shock ahead of the inlet throat. The square and triangle represent data for a choke point at the engine face and for one about 2.5 meters downstream of the engine face, respectively. It is apparent that internal conditions affect the disturbance extent. For unstarts with an engine installed, the diamond represents the extent for an unstart initiated by bypass closure. However, by far the largest disturbance is caused by an unstart resulting from engine stall, which forces boundary-layer separation almost three diameters ahead of the inlet. Therefore, to avoid disturbing an adjacent inlet, its centerline would have to be about three and one-half diameters from the unstarted inlet centerline. It is worth noting again that this requirement is dictated by the extreme extent of the unstart transient and its amplification by the adjacent wing boundary layer. A criteria based on steady-state unstarted conditions without the wing would be totally inadequate.

The unstart not only could disturb adjacent inlets, but also presents a large transient to the engine operation (ref. 13). Unstart normally causes engine stall which can be easily understood by studying figure 20. The left transient is for a mild unstart at Mach 2 where the engine did not stall. The bottom curve of compressor face pressure shows that this pressure drops in about 8 milliseconds. From the center trace, it can be seen that the compressor exit pressure does not stop dropping until about 20 milliseconds after the transient is initiated due to the flow capacitance of the large combustor volume downstream of the compressor. As a result, the compressor pressure ratio increases momentarily to a value near stall but returns to the steady-state pressure ratio as shown in the top trace. Therefore, the transient pressure ratio did not exceed the stall value, and no stall occurred. The middle trace shows a similar case but this time the compressor pressure ratio starts from a higher value, reaches the steady-state stall line during the unstart transient and a stall occurs. The normal steady-state stall line therefore appears to be a valid criteria for engine stall during a transient such as unstart. This may not be surprising since the period for the compressor rotation is about 4 milliseconds. Since in distortion testing the critical distortion angle or rotation angle required for stalling a portion of a parallel compressor is considered to be less than half a compressor rotation, it is not surprising to see the compressor stall at its steady-state stall line during a transient requiring several compressor rotation periods. The traces at the far right are for an inlet unstart and engine stall at $M = 2.5$. While the compressor pressure ratio greatly exceeds the steady-state stall line before stall is reached, the compressor stalls in about 2.5 milliseconds or a little over one-half rotor revolution.

Another transient important to inlet design is the internal inlet overpressure caused by the hammer shock following compressor stall. Several values of this obtained during J-85 inlet tests are presented in figure 21. The figure presents the peak hammer shock static pressure ratioed to the compressor face total pressure \bar{P}_2 just prior to stall. The most important points are the circles for which the compressor stalled at high pressure, \bar{P}_2 , before inlet unstart, causing the highest internal overpressures. However, it is interesting to note the similarity of the pressure ratios obtained from stall after unstart when the compressor inlet pressure, \bar{P}_2 , is about half the higher started value. The data shown correlate well with corrected weight flow per unit frontal area. However, it also correlates well with compressor exit pressure as proposed in reference 14. The overpressure has also been associated with the rate of flow stoppage within the duct during stall (ref. 15). However, this can be a function of duct geometry since compressor interstage and compressor face instrumentation show that compressor stall for the J-85 is not a uniform one-dimensional phenomena, but a progressively growing rotating process. Therefore, in the test inlet which had the subsonic diffuser divided by three struts, the rotating stall process would stop the flow in one third of the duct in about one third of the time required to stop the full duct flow. Therefore, simple approximations to obtain hammer shock overpressure should be used with care.

Since most inlet testing is conducted without an engine present, it is important to determine the effect of the engine on inlet operation. A comparison of inlet distortion measured at similar inlet operating conditions is presented in figure 22. The dashed contours represent coldpipe data where the internal flow system was open from the compressor face station to a choke point about 2.5 meters downstream. The solid lines represent contours with the engine installed. Surprisingly little difference exist between the two total pressure distortions. However, a significant difference can be seen in the static pressures in the three portions of the subsonic diffuser between the centerbody support struts. With the coldpipe installed (dashed underlines) the static pressure in each of the ducts was about equal at the compressor face. With the engine installed, the static pressure in the bottom ducts were lower and the top duct static pressure increased. Therefore, the requirement for constant static pressure in cold pipe testing is changed by the pumping action of the compressor, giving more equal Mach numbers in each duct, reference 16.

Dynamic measurements have also contributed to understanding in the area of inlet distortion effects on compressor operation. In a recent inlet engine test in the 10x10 Foot Supersonic Wind Tunnel, the compressor face was instrumented with six 5-tube rakes which measured both the dynamic pressure variations and the steady-state or time-averaged pressures. During inlet operation at many different conditions, the J-85 engine was purposely stalled to determine the available stall margin. The steady-state and dynamic compressor face pressures were measured before and during stall so that comparisons could be made with steady-state stall parameters obtained from screen distortion testing references 17 and 18.

Distortion from a typical "drift" stall point is shown in figure 23 for a low recovery supercritical condition at zero angle-of-attack. Drift stalls occurred when the engine stalled during a period when no changes were made to any model or engine settings. They occurred most often at fairly high dynamic conditions. The distortion shown on the left is the normal steady-state radial distortion pattern, where the edges between constant density bands represents a line of constant total pressure recovery. Darker regions indicate lower recovery flow. It is a hub radial distortion. The distortion pattern on the right represents the amplitude of the dynamic component of total pressure at the compressor face. This amplitude is presented as the root mean square, rms, of the dynamic pressure component divided by the average compressor face pressure. The rms levels range from less than 0.04 to 0.08 of compressor face average pressure \bar{P}_2 , with an average value of 0.066. Since these pressure fluctuations are random in nature, the peak-to-peak pressure fluctuations can reach four to six times the rms values. Here the darker bands represent higher dynamic pressure levels. It is interesting to note the location of the dynamics relative to the average total pressure bands. In the low total pressure region near the hub, the dynamic levels are lower. The high dynamic region, in this case, corresponds to the higher total pressure region, indicating that the major pressure fluctuations are occurring there.

A similar set of distortion profiles is shown in figure 24 for five degrees angle-of-attack with a total pressure recovery of 0.77. The steady-state circumferential distortion is typical for such an

operating condition with high recovery air at the top, leeward side of the inlet and low pressure air at the bottom. Now, however, the relationship between the high dynamic and high pressure regions is different in this case than for zero angle-of-attack. The dynamic level is again fairly low in the low total pressure region at the bottom of the inlet, but it is at an even lower dynamic level in the high total pressure region at the top of the inlet. In this case, the high dynamics occur between the high and low pressure regions. The different locations of the high dynamic regions in the zero and five degree angle-of-attack case will be discussed again when instantaneous distortions are presented.

In addition to the steady state and rms dynamic distortion plots, the pressure data were simultaneously digitized at a high rate for all thirty probes, and a steady-state distortion parameter and instantaneous distortion contour plots were made. The variation of the steady-state distortion parameter with time for the zero degree angle-of-attack case is presented in figure 25. The time of compressor stall was determined from compressor interstage dynamic pressure data. The parameter presented here is developed in reference 19 and is sensitive only to circumferential distortion, and would have a near zero value for the steady-state distortion pattern of figure 23. However, the instantaneous distortion pattern has an average value of about 0.04 and reaches the critical level required to cause stall once during the observed time span. Therefore, the instantaneous patterns must be considerably different for this case than the time-averaged pattern. A similar presentation of the distortion index variation with time is presented in figure 26 for the five degree angle-of-attack point. Here the average distortion level is higher, as would be expected from the steady-state distortion plot of figure 24. However, it can be seen that the average value is about 35 percent less than the value of 0.15 required for compressor stall. Transiently, however, the distortion does reach and exceed the critical level of distortion several times before compressor stall. A total of twelve stall points have been analyzed in a similar manner and in all but two cases, the time-varying distortion exceeded the critical level required to stall the engine.

To obtain a better understanding of the cause of the large transient distortion levels, an instantaneous contour plot of the peak transient distortion is compared with the steady-state contour in figures 27 and 28 for the zero and five degree angle-of-attack cases. At zero angle-of-attack, (fig. 27) the peak instantaneous distortion is primarily circumferential in nature. The pressures do not change drastically near the hub where the dynamics were low in the rms contour plot. Where the dynamics were high in the steady-state high pressure region, total pressure reaches as much as 20 percent less than the steady-state value in the lower left portion of the inlet. Since the rms contours were nearly symmetrical around the inlet at zero angle-of-attack, a similar pattern could probably occur in any orientation over a long period of time. The dynamics therefore indicated what appear to be large separate regions forming and disappearing which cause major circumferential distortions. A similar comparison of the instantaneous and steady-state distortion contours for five degrees angle-of-attack are presented in figure 28. Here the two contour plots are very similar, with the instantaneous plot having a broader high pressure region and lower pressure at the bottom of the inlet. Both effects tend to increase the circumferential distortion. The high dynamic regions were observed between the high and low pressure regions on the rms contour plots, and this can be correlated with the constant total pressure boundaries expanding and contracting across this region. Lower dynamics were observed at the top and bottom of the inlet where the high and low pressure region remain stably located, but vary somewhat in level.

Therefore inlet dynamics are apparently associated with unstable flow in the diffuser and not with turbulence in the classical sense. The dynamic level is not associated with any particular region of the steady-state distortion pattern. It is associated with the high pressure flow region passing back and forth over the measurement point as flow which is separating and attaching to a wall might do. This is a recognized operational regime for subsonic diffusers, reference 20. Therefore, the probable cause of most of the dynamic distortion measured in inlets, is transient flow separation in the subsonic diffuser combined with the terminal shock boundary layer interaction. Hence test techniques are required which determine if significant dynamic distortion is present, and if so, enough dynamic instrumentation is required to determine the instantaneous distortion pattern.

CONCLUDING REMARKS

Most wind tunnel testing of supersonic exhaust nozzles is done to obtain off design performance in the speed range near Mach 1.0. Because of the complex internal and external flows, it is very difficult to duplicate all conditions simultaneously. It has been demonstrated that jet boundary simulators can provide good data if the flow is well behaved in the nozzle region. However, if separation is present, this method would probably become suspect. Then more complex models such as powered simulators should be used. Results from such a model were compared with flight data and were shown to agree up to high subsonic Mach numbers. However, viscous effects can still affect the nozzle drag and full Reynolds number testing is currently impossible in existing facilities. Two cases were presented where boundary-layer thickness affected the drag in opposite directions and demonstrated the need to fully understand the flow conditions. The viscous effects area is not completely understood yet and work in this area is continuing at Lewis.

Dynamic measurements are absolutely necessary to understand the interactions of an inlet-engine combination. Nacelle spacing is determined by a maximum transient disturbance extent during unstart that is much larger than the steady-state disturbance. Engine stall during inlet unstart was easily explained by utilizing dynamic measurements of compressor pressure ratio. Nacelle strength is partially determined by the overpressures due to the hammer shock after compressor stall and it must be carefully measured with dynamic instrumentation. Probably the most complex flow phenomena revealed by dynamic measurements is dynamic distortion. Proper reduction of dynamic distortion data holds promise for explaining inlet-engine compatibility in terms of comparing the instantaneous distortion with the steady-state screen distortion required to stall the compressor. Several cases were presented demonstrating the nature of the flow fluctuations for different inlet operating conditions. The number of cases investigated so far has been limited due to the difficulty of data reduction but this is becoming easier with new methods. Work is continuing at Lewis on dynamic distortion, and should provide further understanding of the dynamic interaction of the inlet and engine.

REFERENCES

1. Beheim, Milton A.; Anderson, Bernhard H.; Clark, John S.; Corson, Blake W., Jr.; Stitt, Leonard E.; and Wilcox, Fred A.: Supersonic Exhaust Nozzles. Aircraft Propulsion. NASA SP-259, 1971, pp. 233-282.
2. Bowditch, David N.; Coltrin, Robert E.; Sanders, Bobby W.; Sorensen, Norman E.; and Wasserbauer, Joseph F.: Supersonic Cruise Inlets. Aircraft Propulsion. NASA SP-259, 1971, pp. 283-312.
3. Povolny, John H.; Burcham, F. W., Jr.; Calogeras, James E.; Meyer, Carl L.; and Rudey, Richard A.: Effects of Engine Inlet Disturbances on Engine Stall Performance. Aircraft Propulsion. NASA SP-259, 1971, pp. 313-349.
4. Harrington, Douglas E.: Jet Effects on Boattail Pressure Drag of Isolated Ejector Nozzles at Mach Numbers From 0.60 to 1.47. NASA TM X-1785, 1969.
5. Wilcox, Fred A.; Samanich, Nick E.; and Blaha, Bernard J.: Flight and Wind Tunnel Investigation of Installation Effects on Supersonic Cruise Exhaust Nozzles at Transonic Speeds. 69-427, AIAA, June 1969.
6. Samanich, Nick E.; and Burley, Richard R.: Flight Performance of Auxiliary Inlet Ejector and Plug Nozzle at Transonic Speeds. Paper 70-701, AIAA, June 1970.
7. Mikkelsen, Daniel C.; and Head, Verlon L.: Flight Investigation of Airframe Installation Effects on a Variable Flap Ejector Nozzle of an Under wing Engine Nacelle at Mach Numbers From 0.5 to 1.3. NASA TM X-2010, 1970.
8. Mikkelsen, Daniel C.; and Blaha, Bernard J.: Flight and Wind Tunnel Investigation of Installation Effects on Underwing Supersonic Cruise Exhaust Nozzles at Transonic Speeds. Presented at the AGARD Aerodynamic Interference Specialists Meeting, Silver Spring, Md. Sept. 28-30, 1970.

9. Groth, Harold W.: Nozzle Performance Measurements on Underwing Nacelles of an F-106 Utilizing Calibrated Engines and Load Cells. Paper 71-681, AIAA, June 1971.
10. Blaha, Bernard J.; and Bresnahan, Donald L.: Wind Tunnel Installation Effects on Isolated Afterbodies at Mach Numbers From 0.56 to 1.5. NASA TM X-52581, 1969.
11. Mitchell, Glenn A.; and Johnson, David F.: Experimental Investigation of the Interaction of a Nacelle-Mounted Supersonic Propulsion System with a Wing Boundary Layer. NASA TM X-2184, 1971.
12. Johnson, David F.; and Mitchell, Glenn A.: Experimental Investigation of Two Methods for Generating an Artificially Thickened Boundary Layer. NASA TM X-2238, 1971.
13. Choby, David A.; Burstadt, Paul L.; and Calogeras, James E.: Unstart and Stall Interactions Between a Turbojet Engine and an Axisymmetric Inlet With 60-Percent Internal-Area Contraction. NASA TM X-2192, 1971.
14. Bellman, Donald R.; and Hughes, Donald L.: The Flight Investigation of Pressure Phenomena in the Air Intake of an F-111 A Airplane. Paper 69-488, AIAA, June 1969.
15. Mays, Ronald A.: Inlet Dynamics and Compressor Surge. Paper 69-484, AIAA, June 1969.
16. Coltrin, Robert E.; and Choby, David A.: Steady-State Interactions From Mach 1.98 to 2.58 Between a Turbojet Engine and an Axisymmetric Inlet With 60 Percent Internal Area Contraction. NASA TM X-1780, 1969.
17. Calogeras, James E.; Mehalic, Charles M.; and Burstadt, Paul L.: Experimental Investigation of the Effect of Screen-Induced Total Pressure Distortion on Turbojet Stall Margin. NASA TM X-2239, 1971.
18. Calogeras, James E.; Burstadt, Paul L.; and Coltrin, Robert E.: Instantaneous and Dynamic Analysis of Supersonic Inlet-Engine Compatibility. Paper 71-667, AIAA, June 1971.
19. Calogeras, James E.; Mehalic, Charles M.; and Burstadt, Paul L.: Experimental Investigation of the Effect of Screen-Induced Total-Pressure Distortion on Turbojet Stall Margin. NASA TM X-2239, March 1971.
20. Sovran, Gino; and Klomp, Edward D.: Experimentally Determined Optimum Geometries for Rectilinear Diffusers with Rectangular, Conical or Annular Cross-Section. Fluid Mechanics of Internal Flow. Gino Sovran, ed., Elsevier Publ. Co., 1967, pp. 270-319.

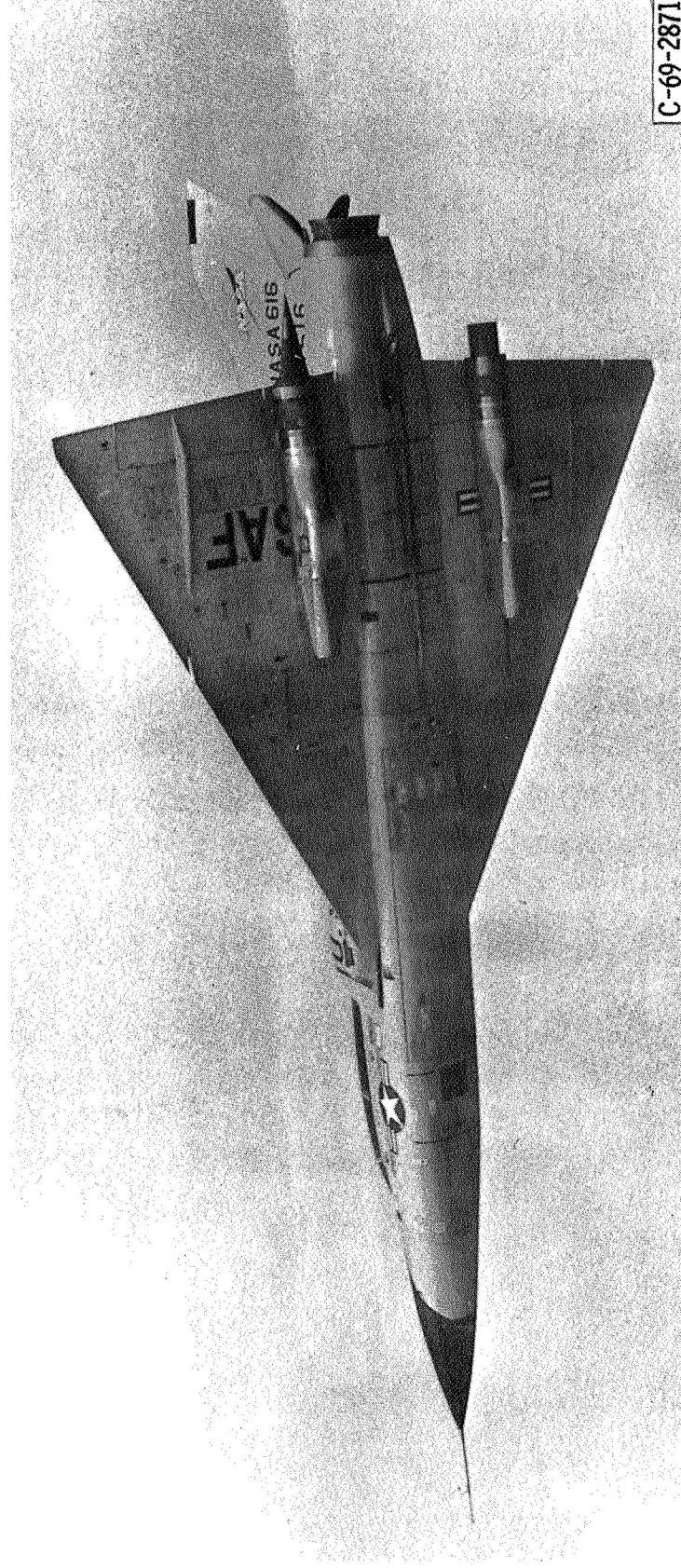
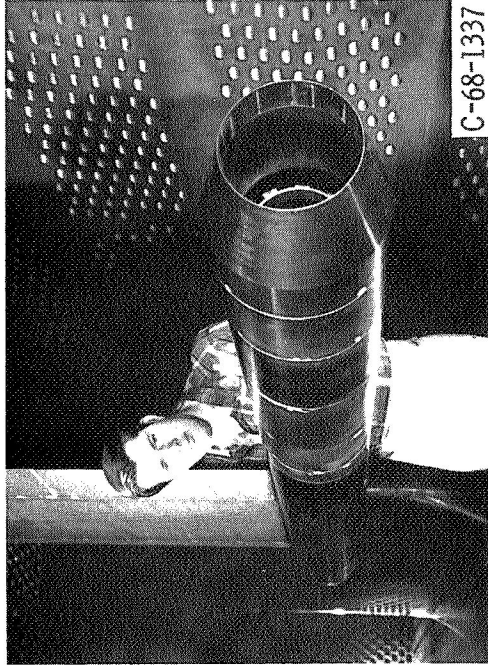
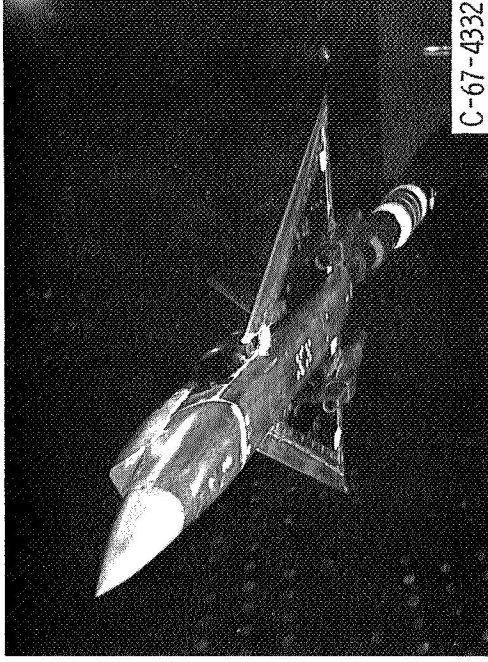


Figure 1. - F-106 research flight with plug nozzle.

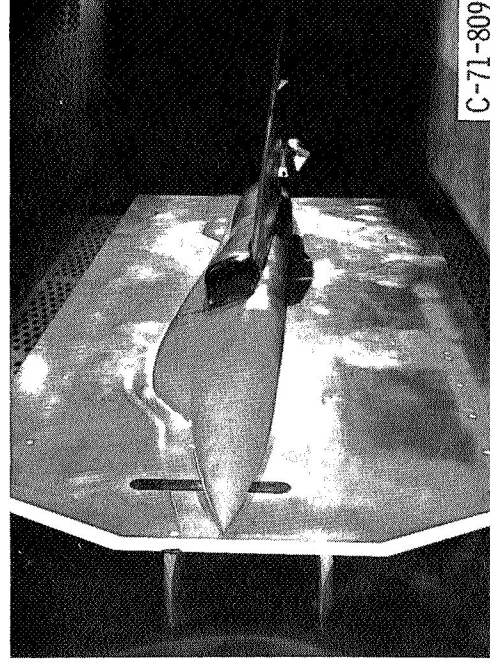
E-6416



ISOLATED NOZZLE



5% SCALE F-106



22% SCALE F-106

Figure 2. - Exhaust nozzle test models.

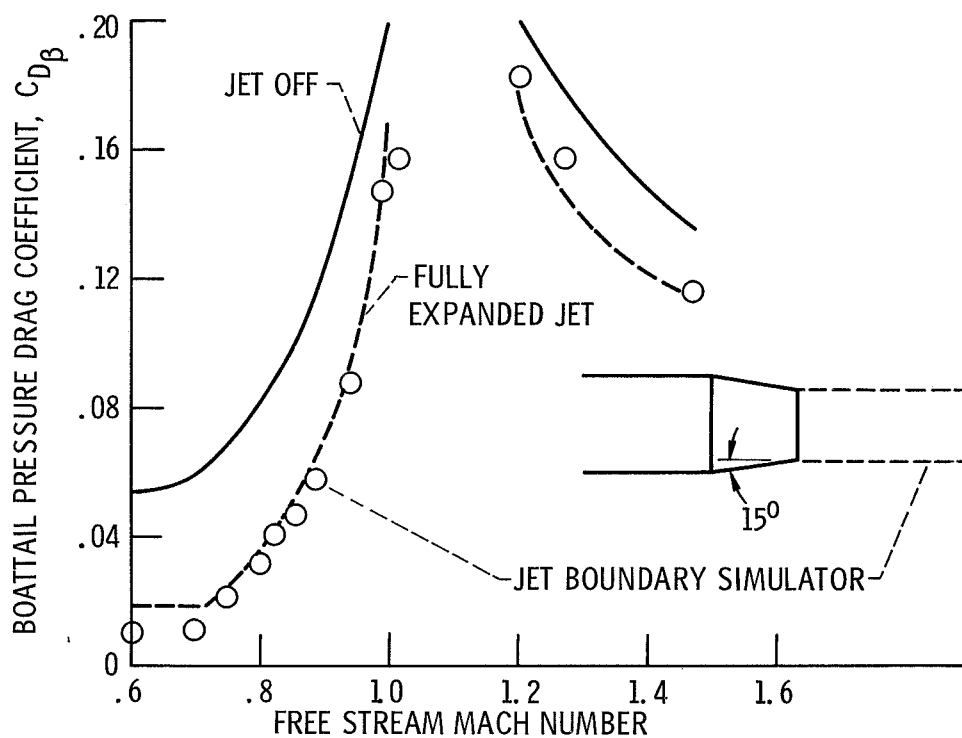
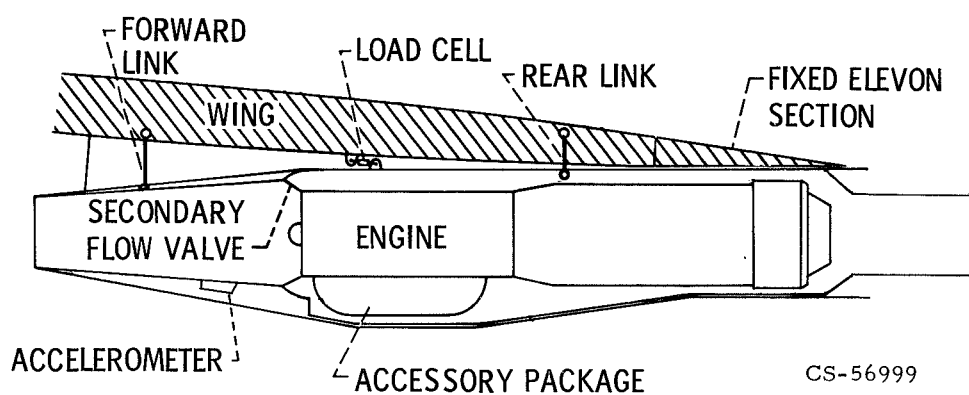


Figure 3. - Comparison of boattail drag for jet boundary simulator and jet on and off.



CS-56999

Figure 4. - Nacelle-engine installation.

PARAMETER	INFLUENCE COEFFICIENT FOR C_g	STANDARD DEVIATION σ
EXPERIMENTAL NACELLE TARE	0.598	1.50
IDEAL THRUST (GAS GENERATOR)	.994	1.11
LOAD CELL FORCE	.395	1.00
NOZZLE GROSS THRUST COEFFICIENT, C_g		1.47

Figure 5. - F106 Nozzle performance measurement accuracy.

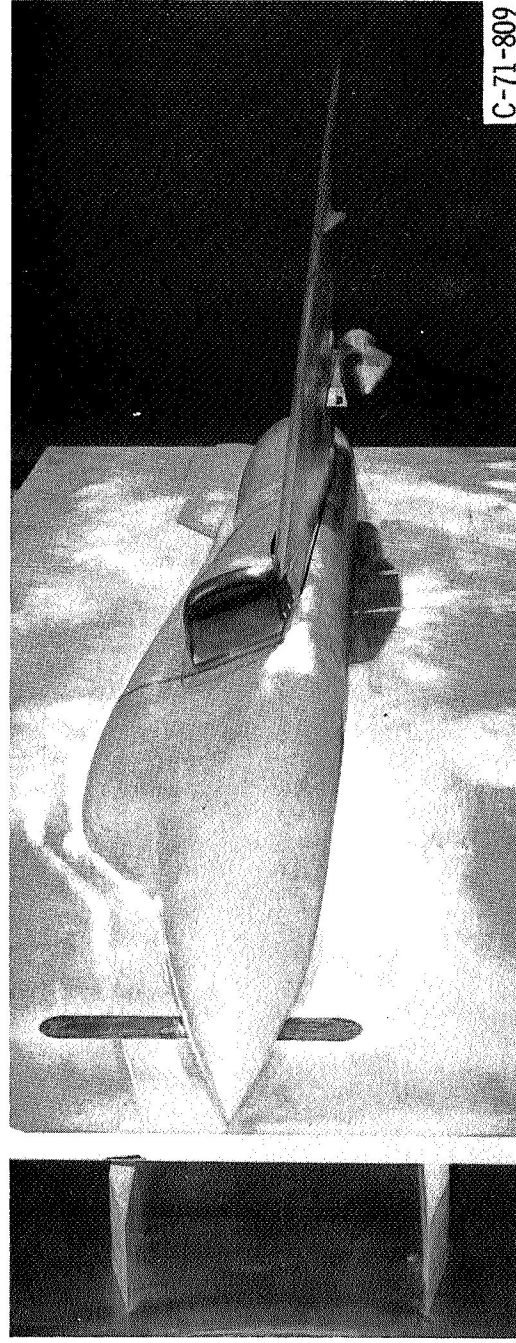
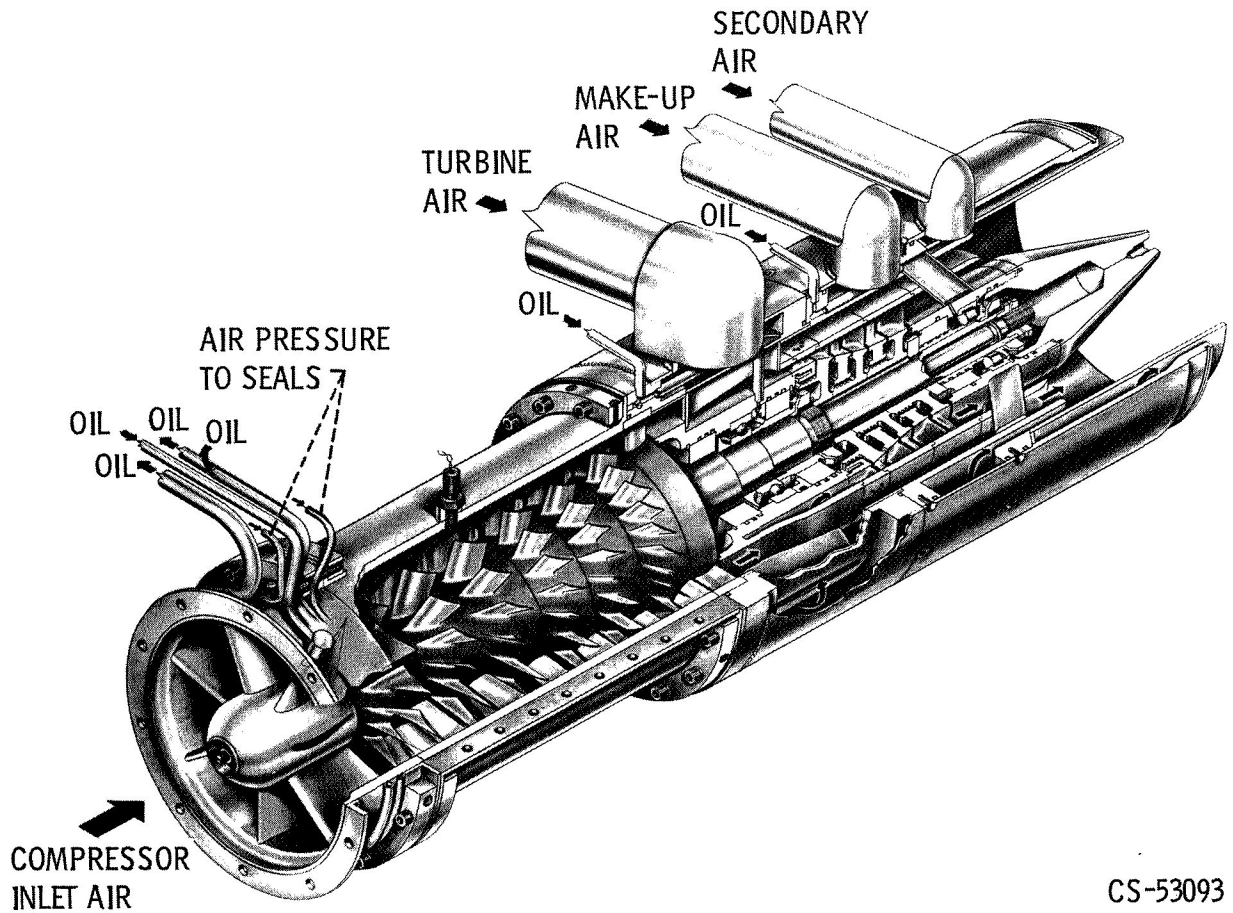
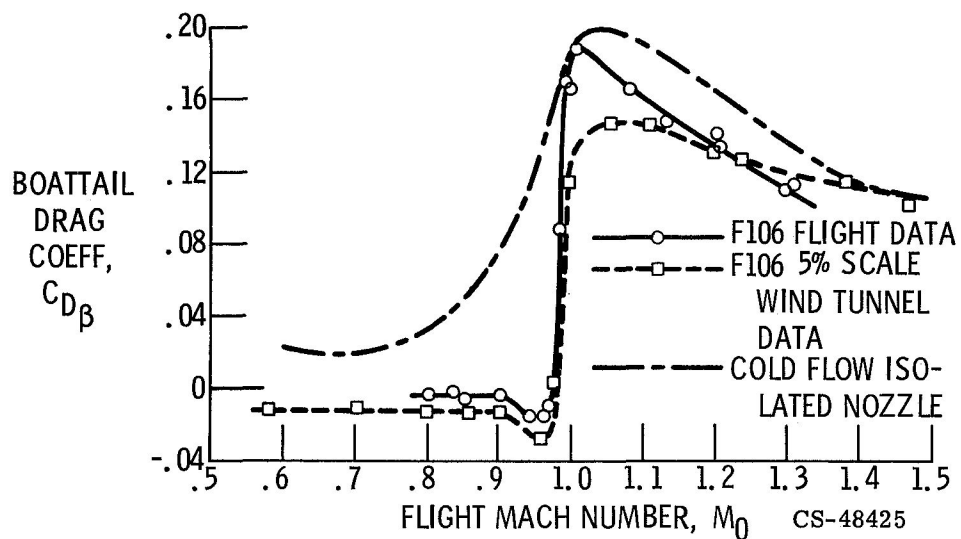


Figure 6. - 22% F-106 model.



CS-53093

Figure 7. - Turbojet engine simulator.

Figure 8. - Comparison of flight and wind tunnel data.
Variable flap ejector nozzle $r/d_n = 0$.

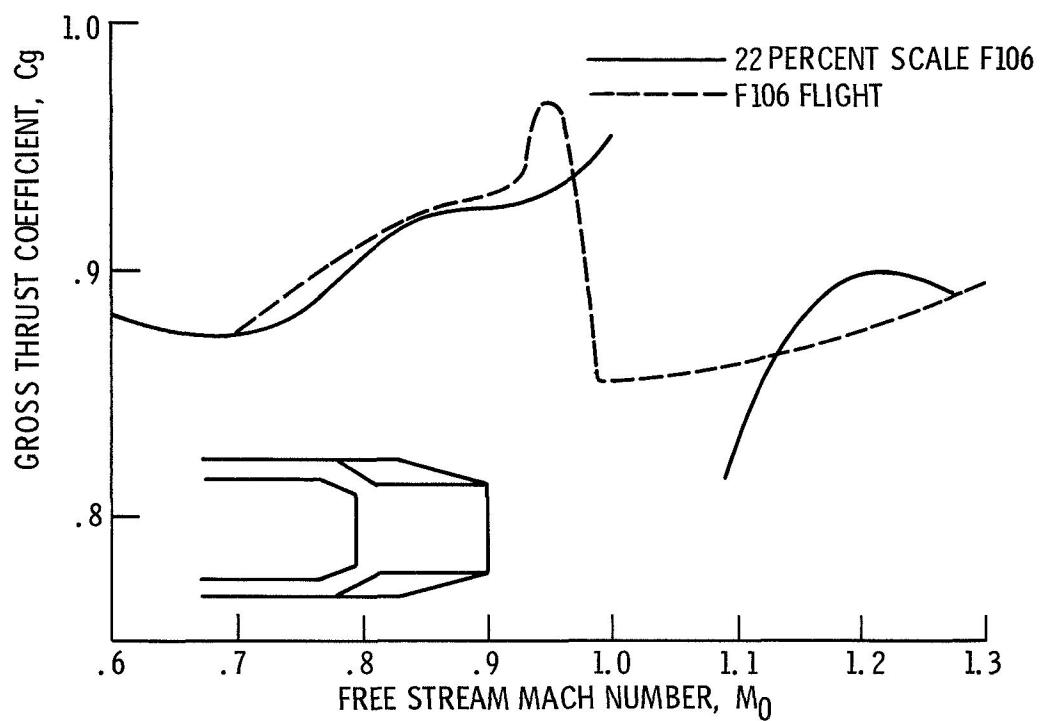


Figure 9. - Comparison of variable flap ejector performance from model and flight data.

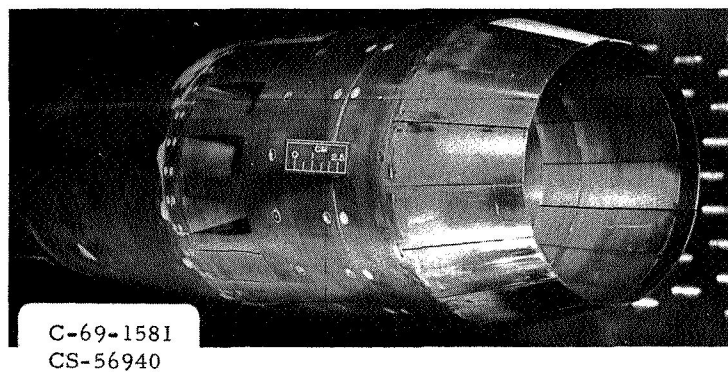
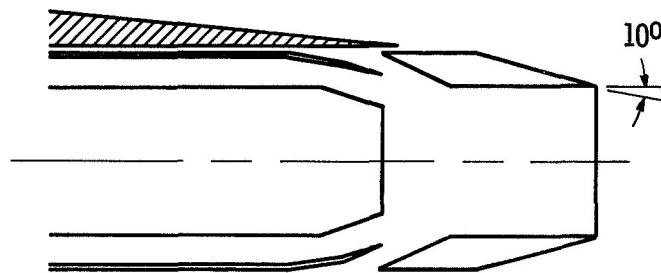


Figure 10. - Auxiliary inlet ejector.

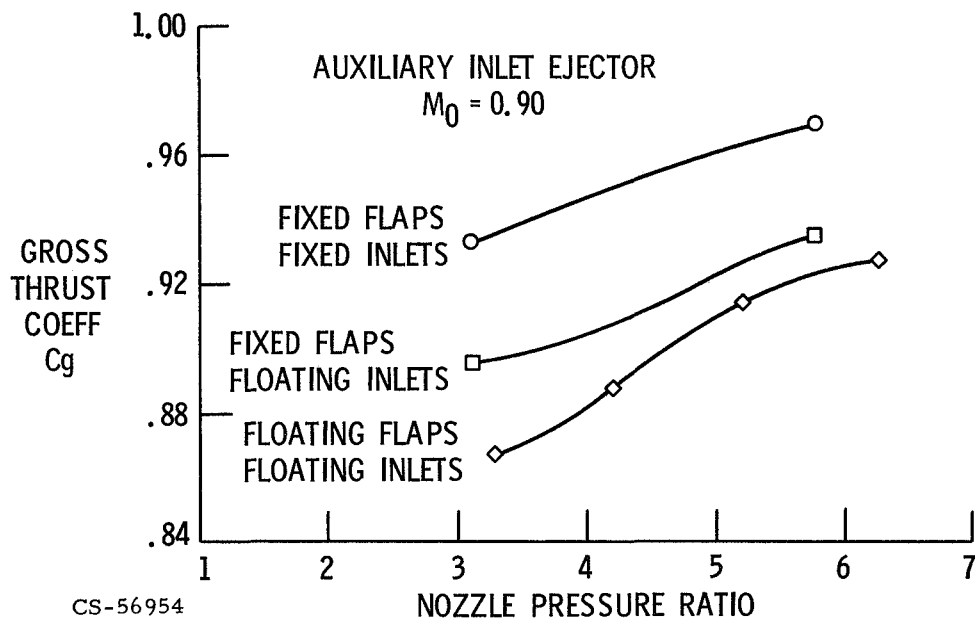
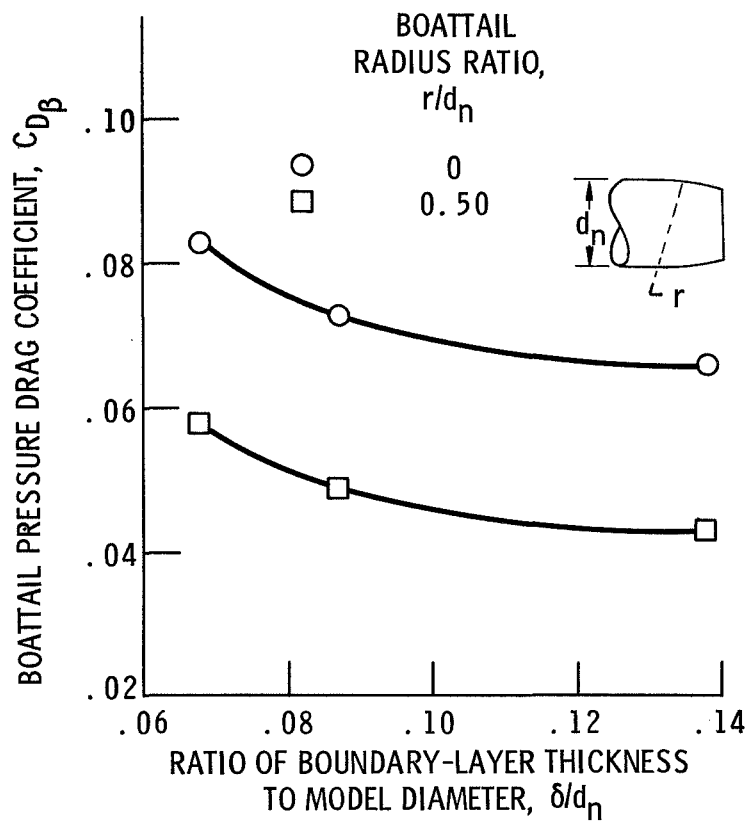
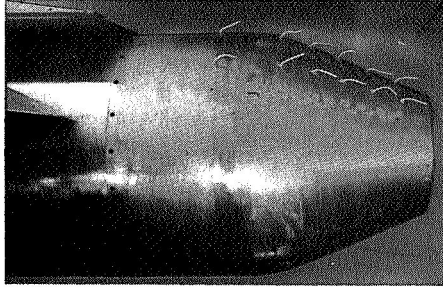
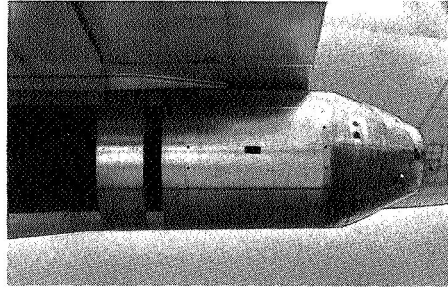


Figure 11. - Effect of floating components on performance.

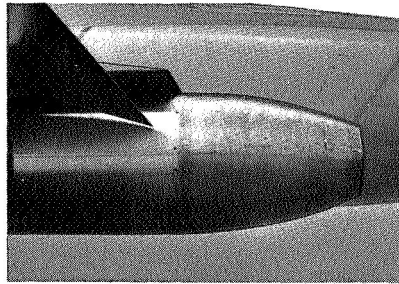
Figure 12. - Effect of boundary-layer thickness on boattail pressure drag; 15° - conical boattails at Mach 0.90.



CASE 1 - $r/d_n = 0.72$ EXTENDED 1/2 DIAM



CASE 2 - $r/d_n = 0.72$



CASE 3 -
CIRCULAR ARC

CS-57004

Figure 13. - Variable convergent-divergent nozzles.

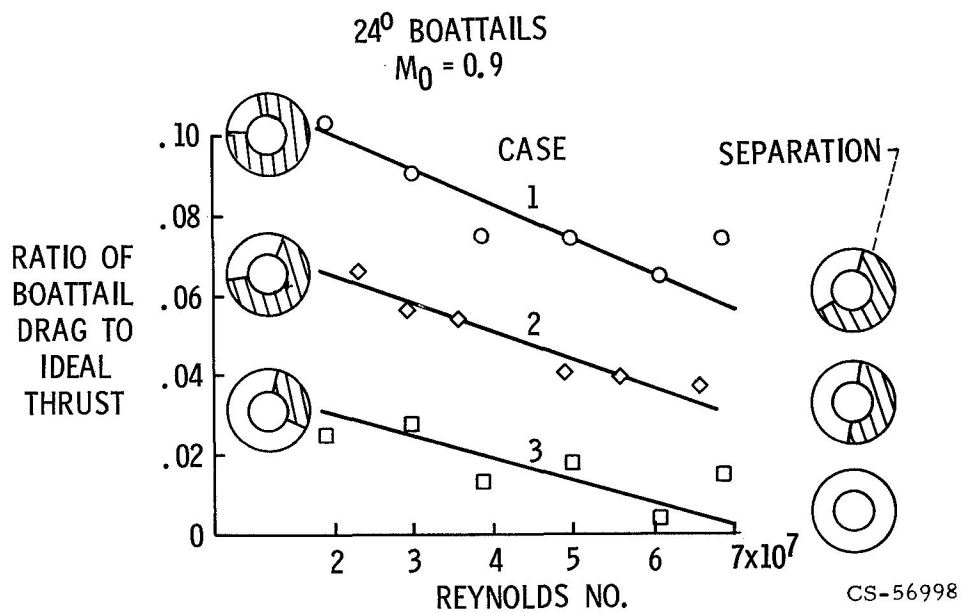


Figure 14. - Reynolds number effect on boattail drag.

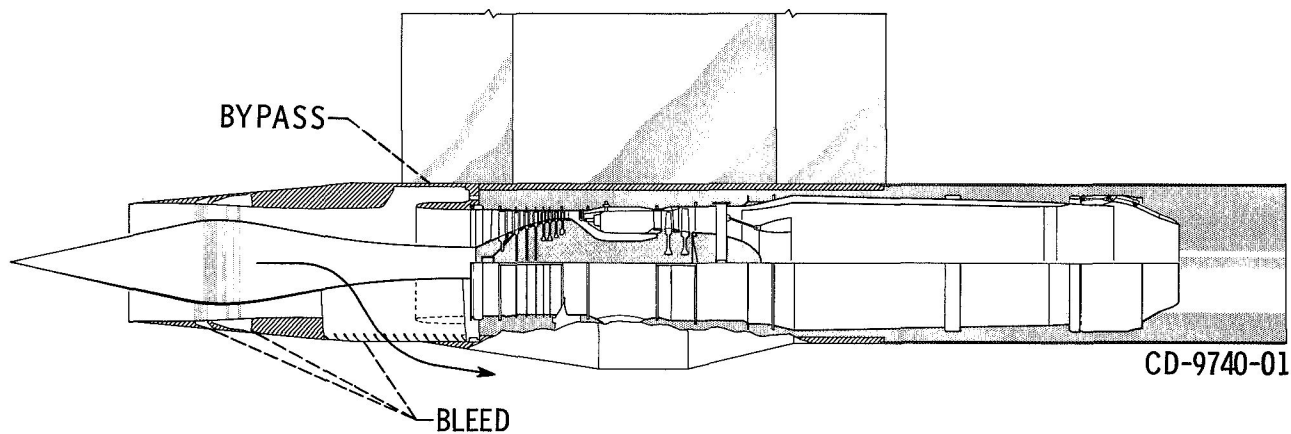
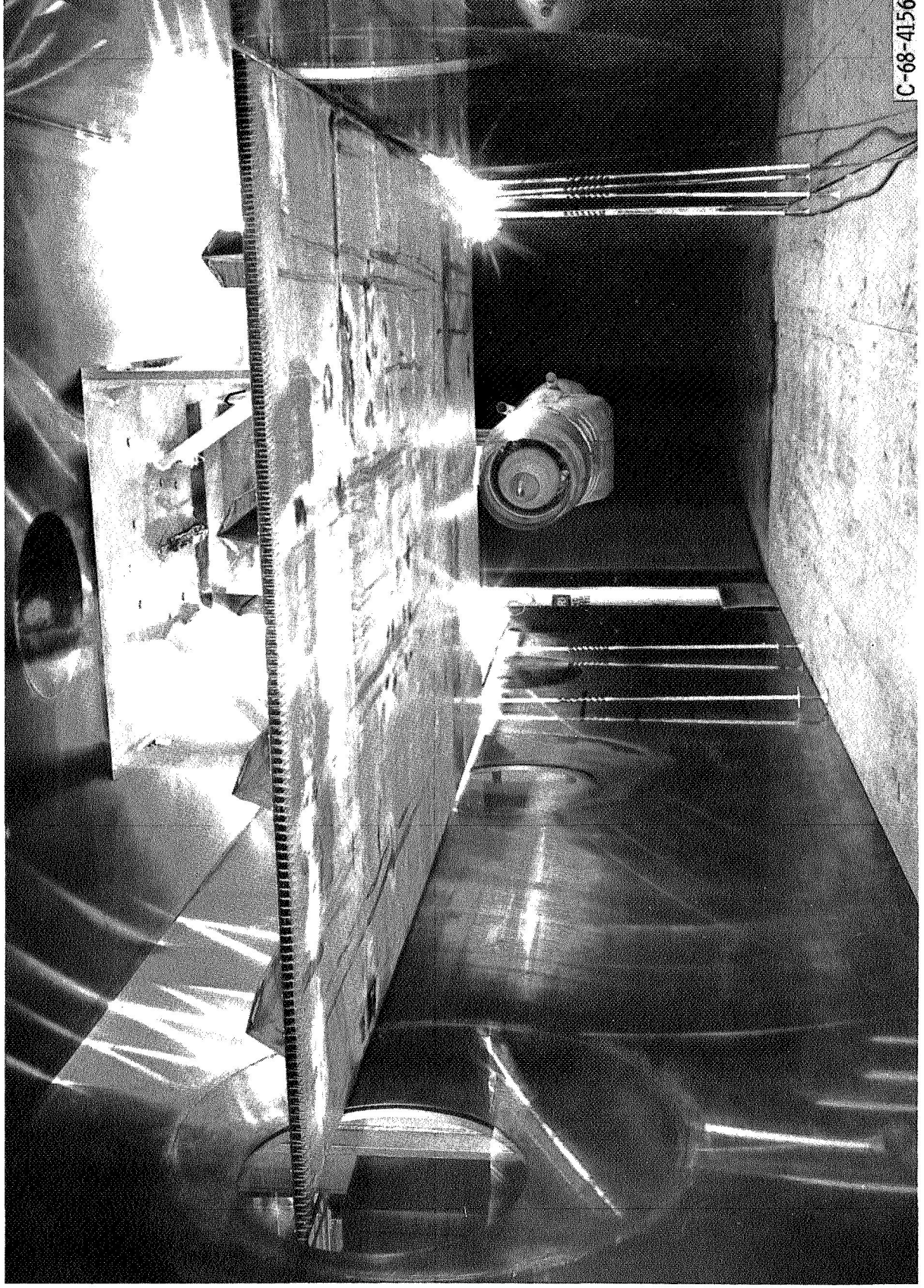


Figure 15. - Axisymmetric mixed compression and J85 turbojet installation.



C-68-4156

Figure 16. - Propulsion system and wing simulator installation in 10-by 10.

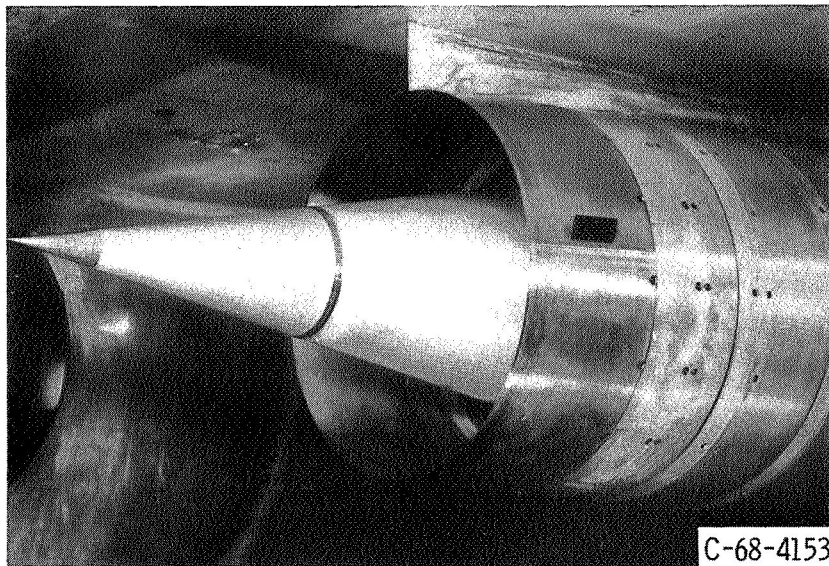


Figure 17. - Inlet location near wing simulator.

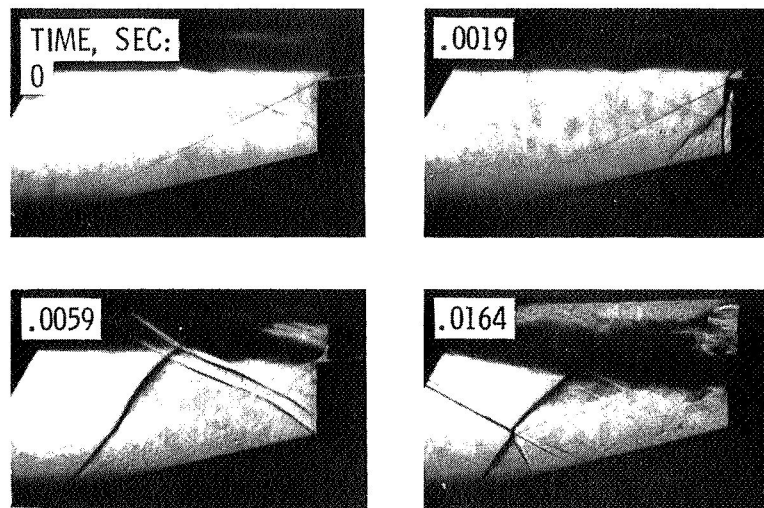


Figure 18. - Inlet unstart near a wing; $Mo = 2.5$.

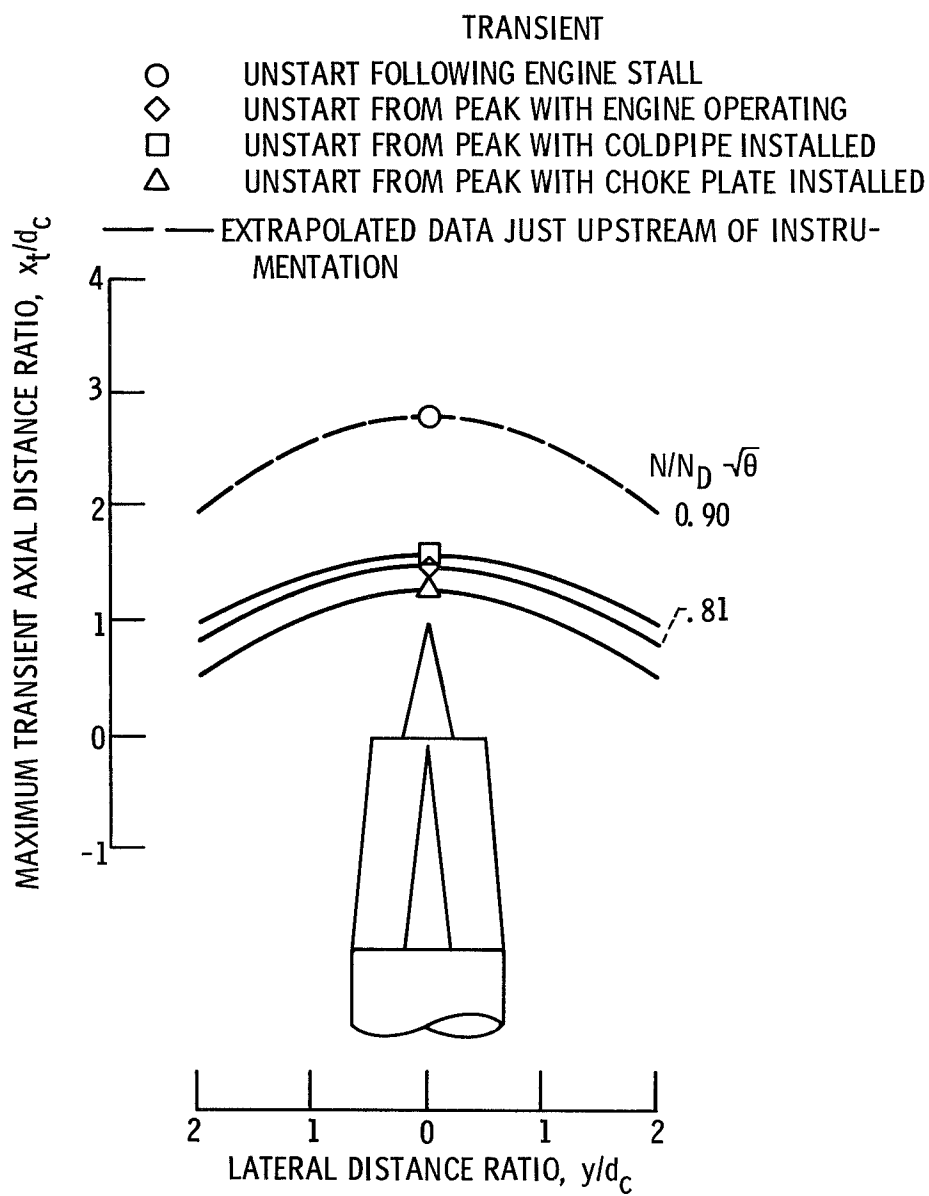


Figure 19. - Maximum wing surface disturbances during inlet unstart transients. $M_0 = 2.5$.

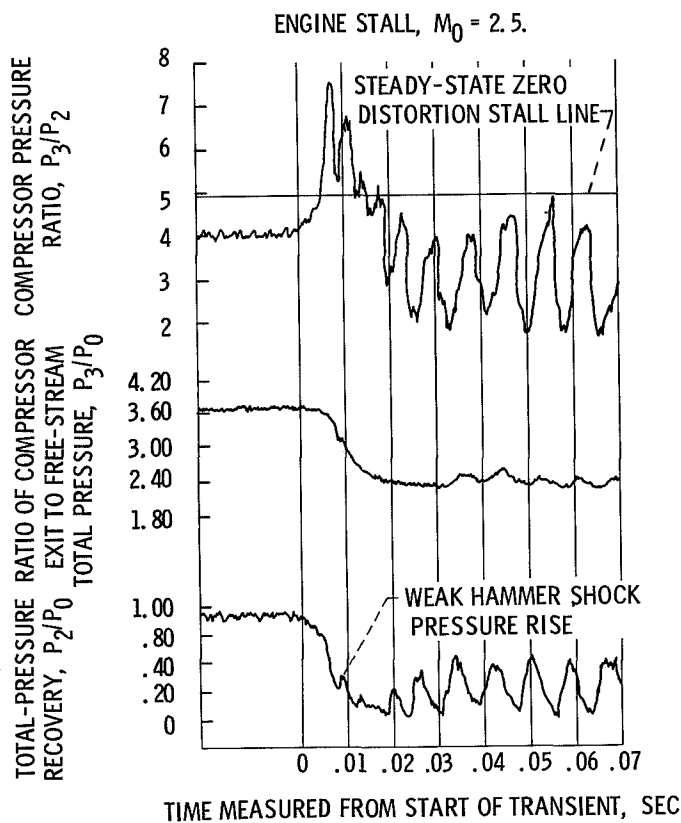
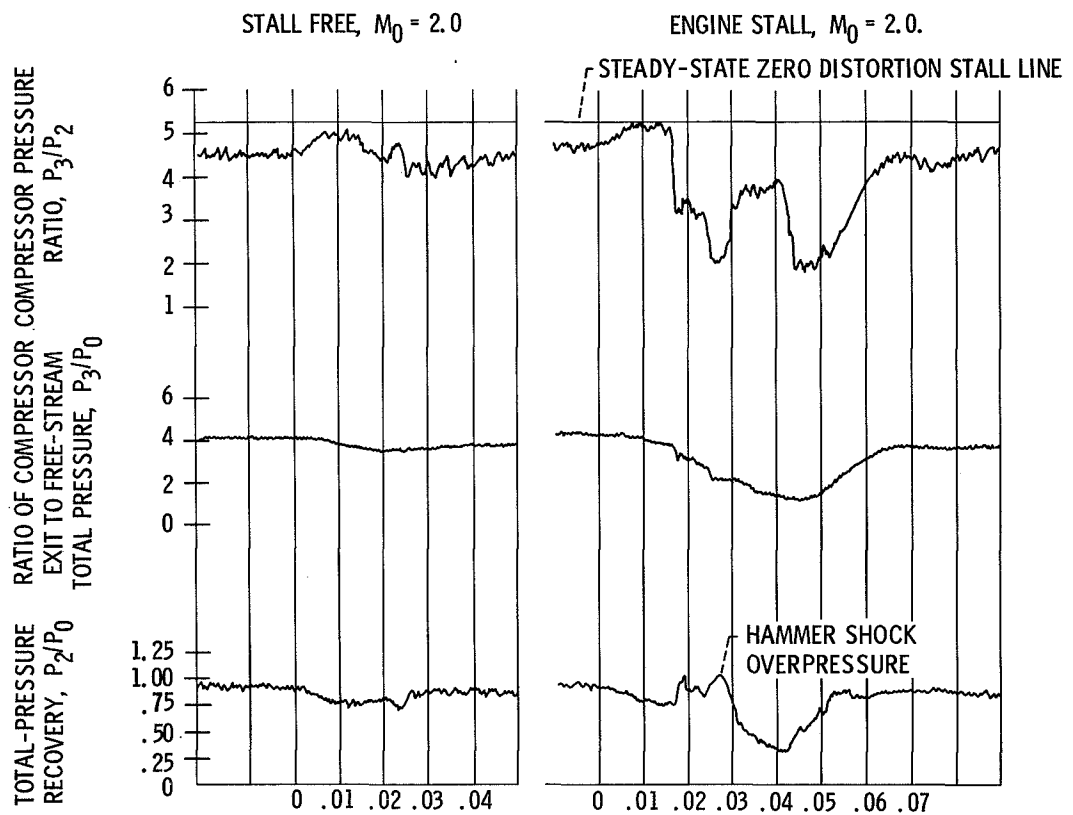


Figure 20. - Effect of inlet unstart on turbojet engine stability.

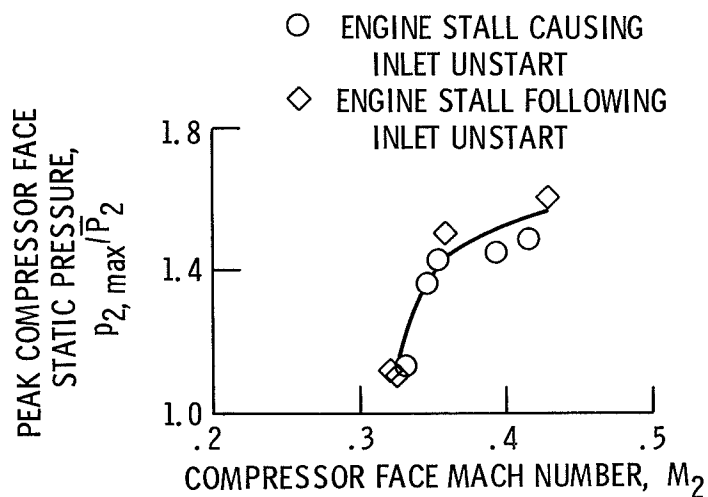


Figure 21. - Hammershock peak pressure following compressor stall.

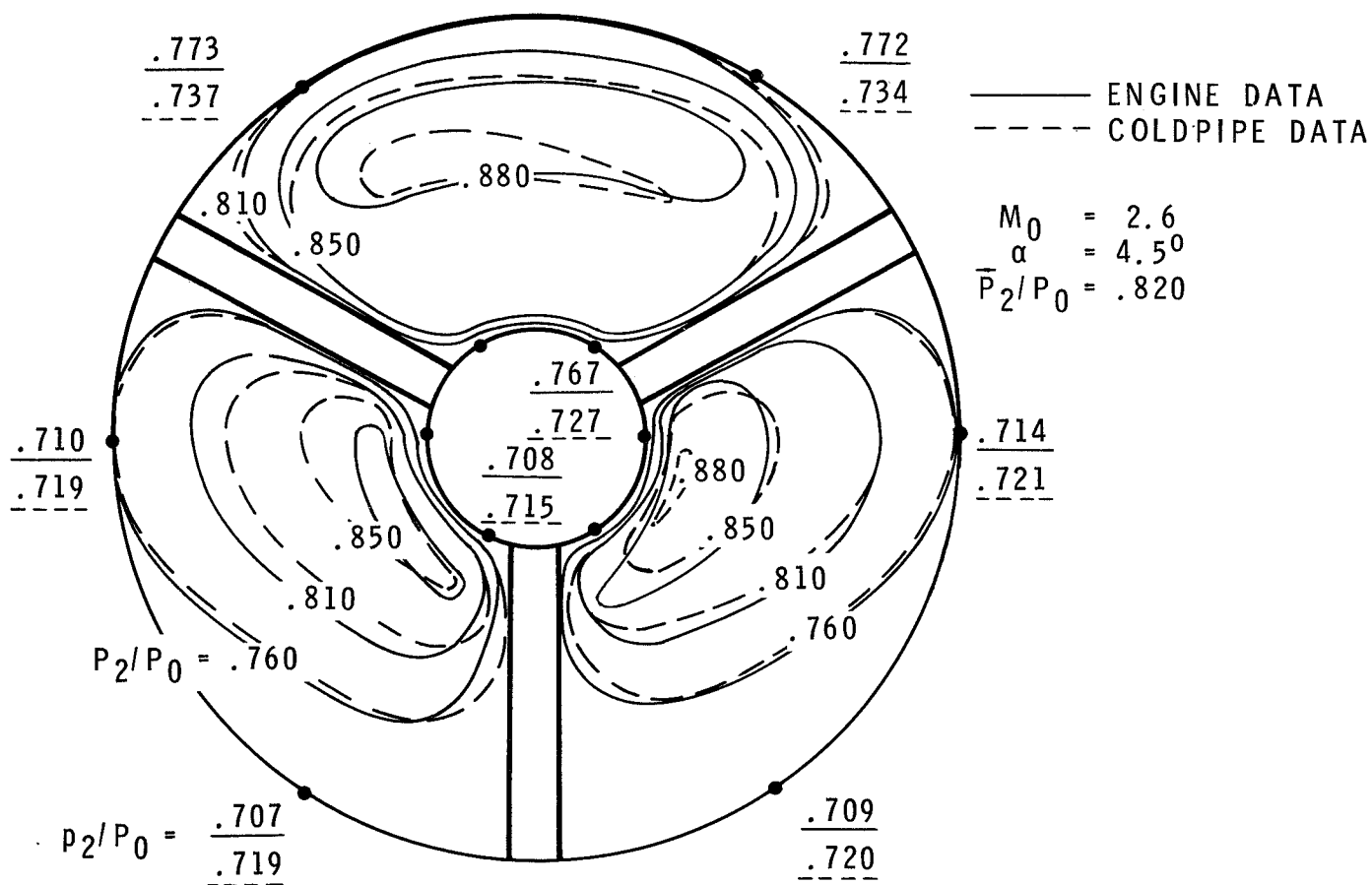
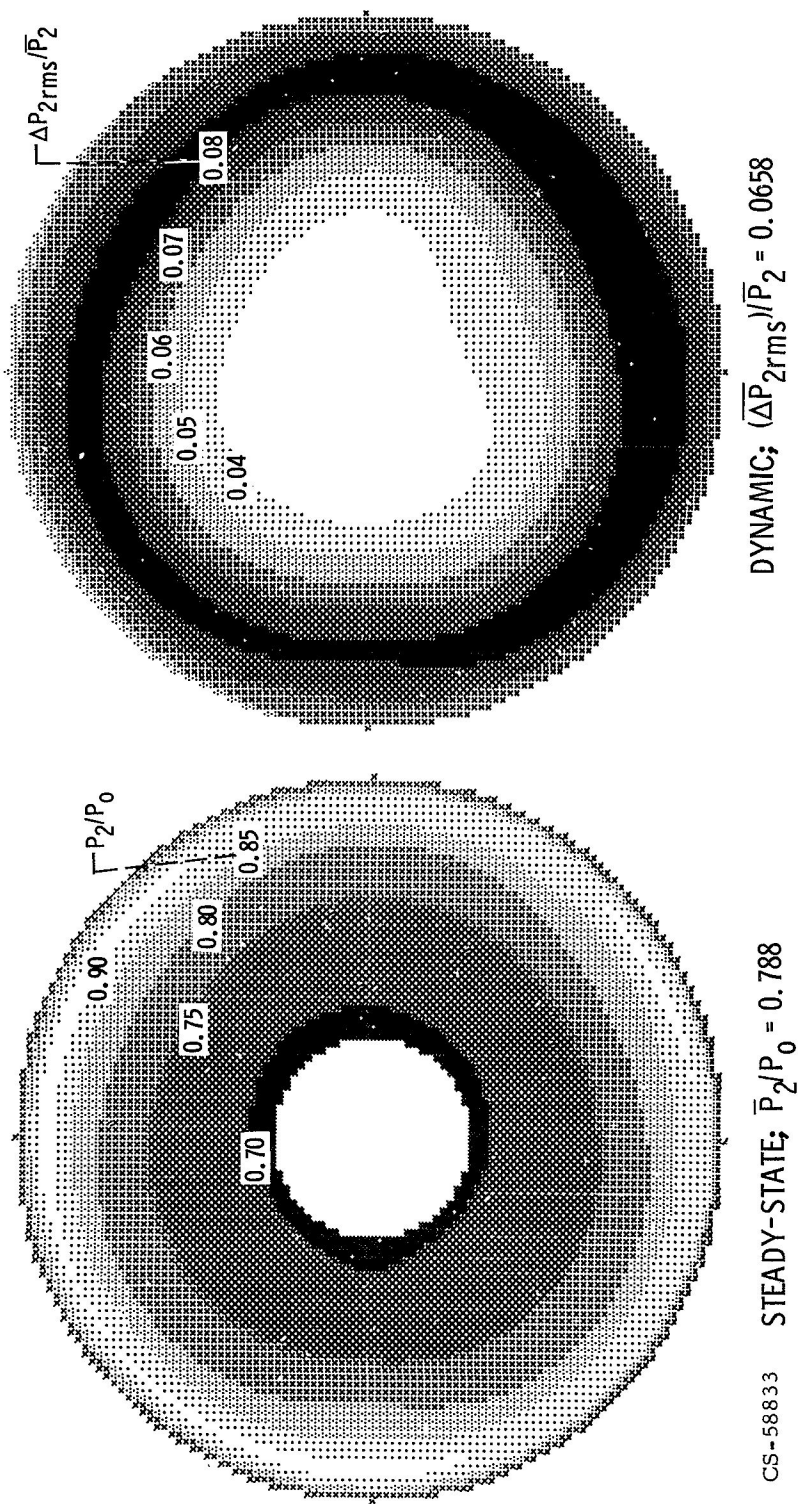
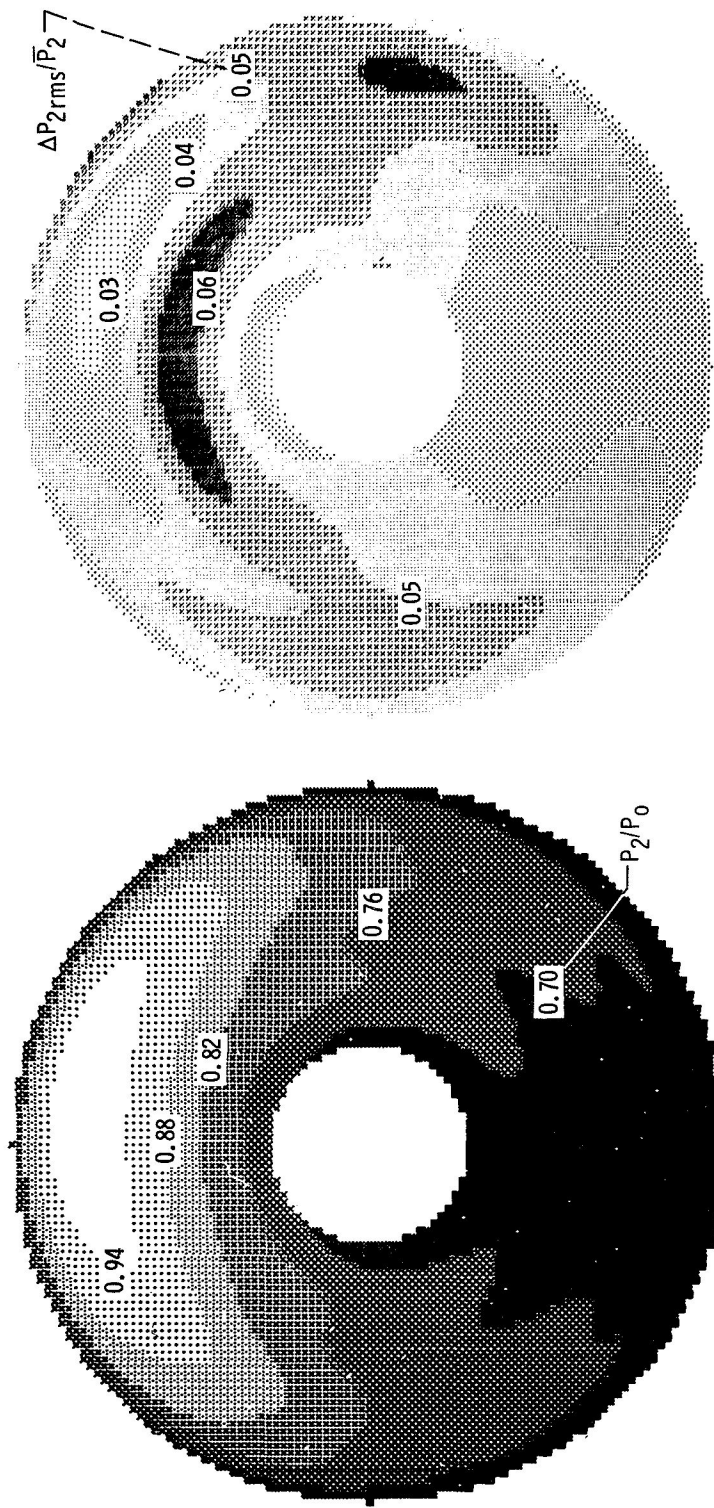


Figure 22. - Engine effect on distortion.





CS-58832 STEADY-STATE; $\bar{P}_2/P_0 = 0.769$

DYNAMIC; $(\Delta P_{2rms})/\bar{P}_2 = 0.046$

Figure 24. - Dynamic and steady state distortion. $M_0 = 2.6$; 5° angle of attack.

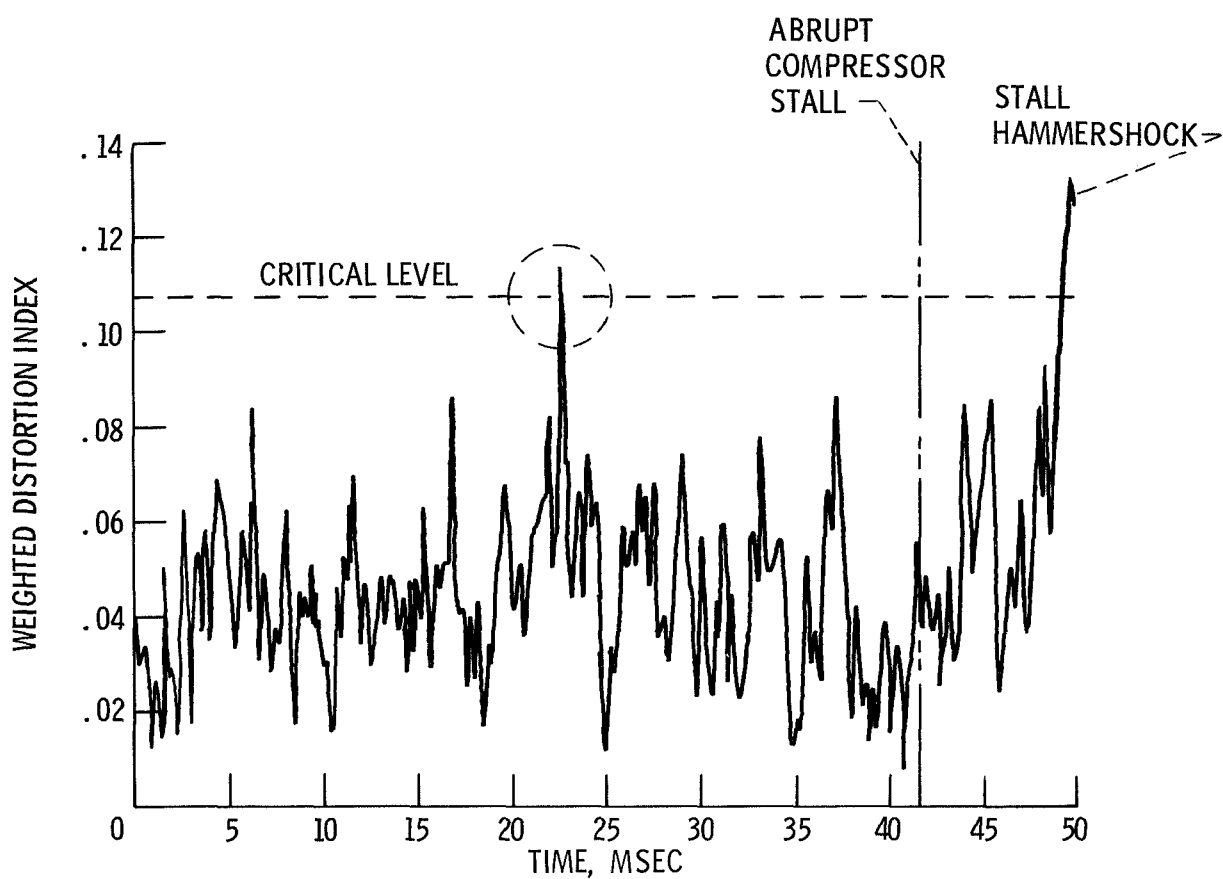


Figure 25. - Instantaneous distortion just prior to compressor stall. $M_0 = 2.5$; 0° angle of attack.

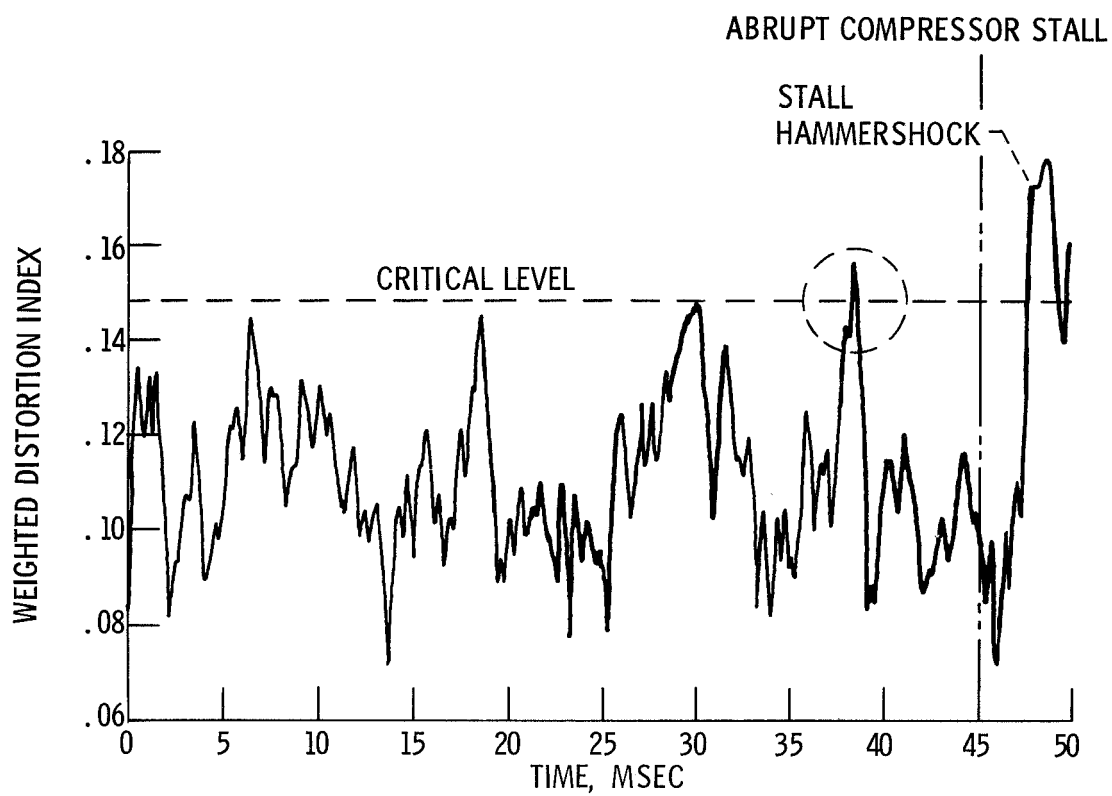


Figure 26. - Instantaneous distortion just prior to compressor stall. $M_0 = 2.6$; 5° angle of attack.

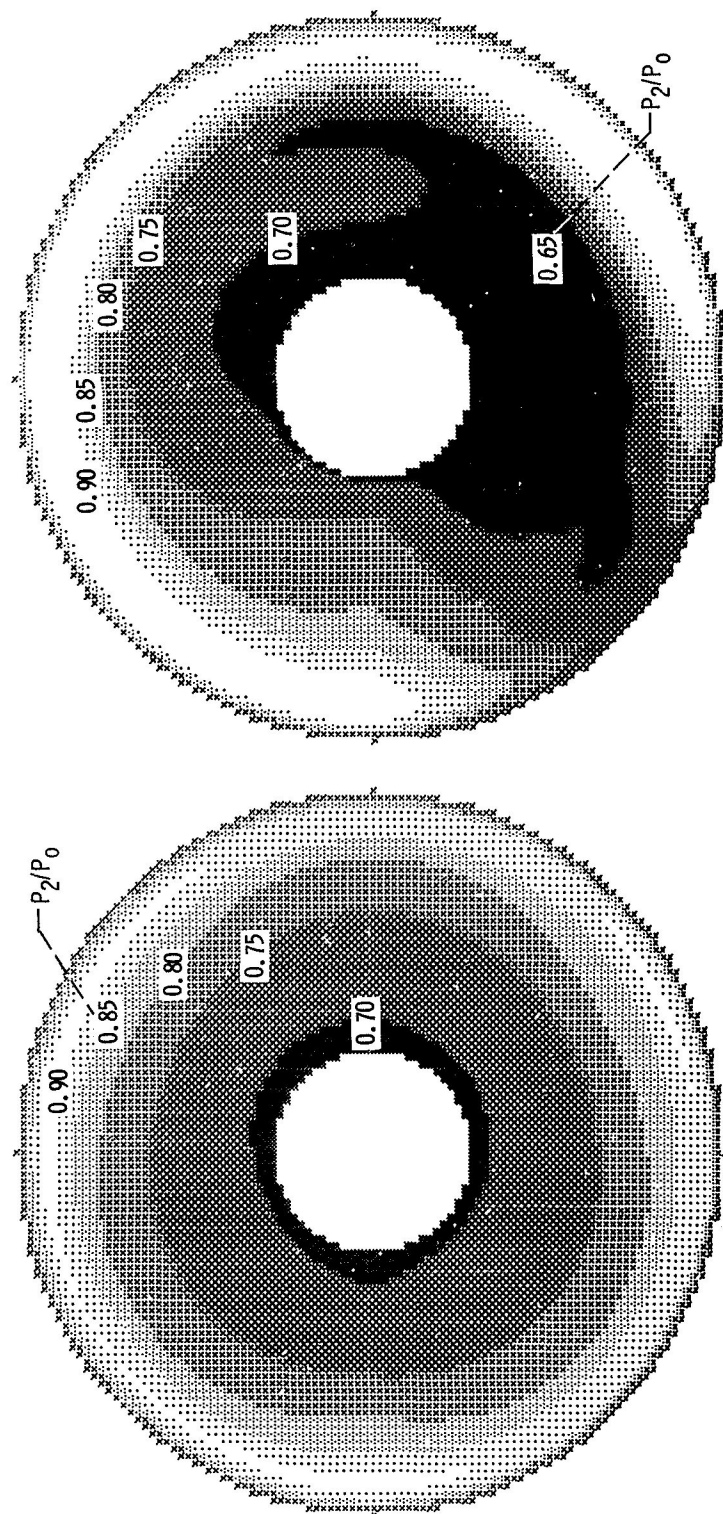
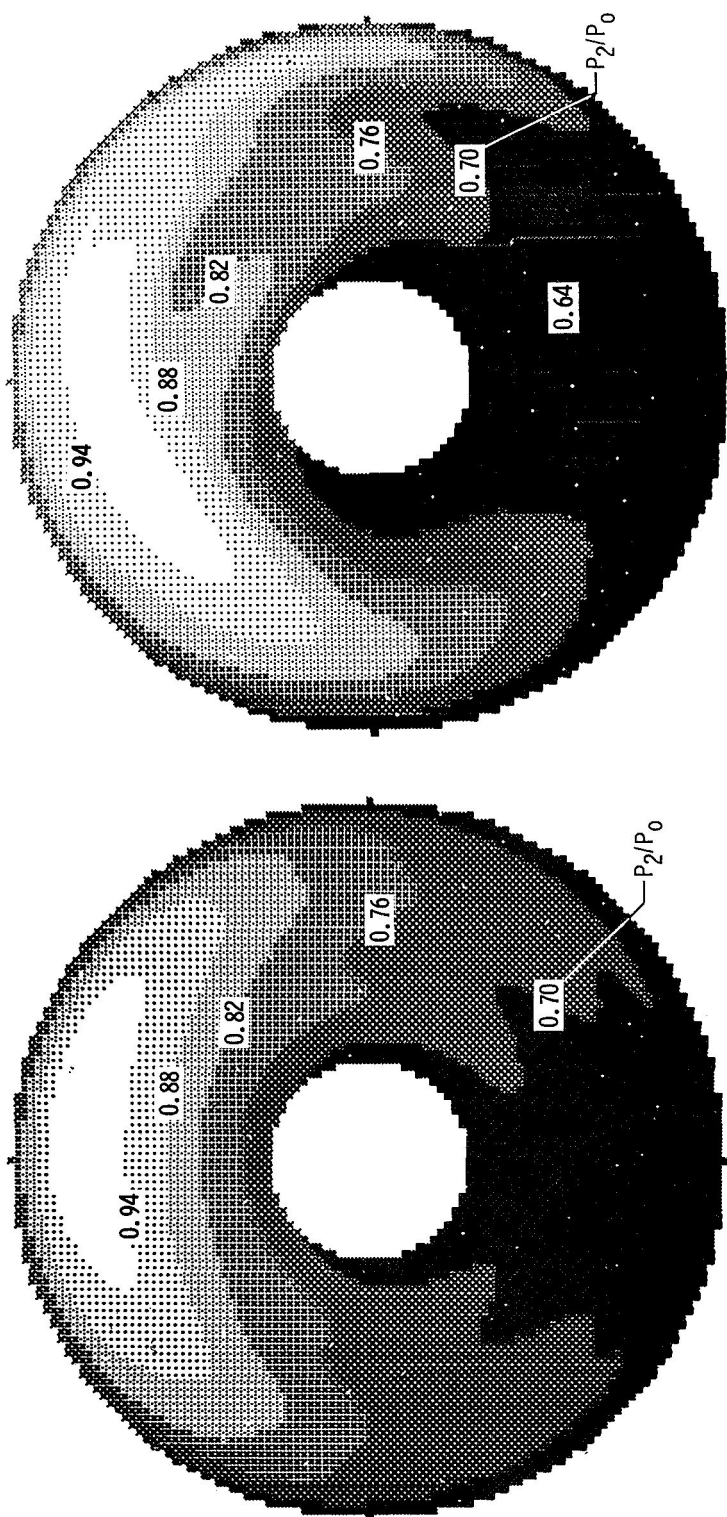


Figure 27. - Comparison of steady state and peak instantaneous distortion. $M_0 = 2.5$; 0° angle of attack.



CS-58831 STEADY-STATE; $\bar{P}_2/P_0 = 0.769$ PEAK INSTANTANEOUS; TIME = 38.50 mSEC

Figure 28. - Comparison of steady state and peak instantaneous distortion. $M_0 = 2.6$; 5° angle of attack.